THE JOURNAL OF
PHYSICAL CHEMISTRY C

pubs.acs.org/JPCC Article

Enhanced Inorganic $CsPbIBr_2$ Perovskite Film for a Sensitive and Rapid Response Self-Powered Photodetector

Vincent Obiozo Eze, Geoffrey Ryan Adams, Lucas Braga Carani, Ryan James Simpson, and Okenwa I. Okoli*

Cite This: *J. Phys. Chem. C* 2020, 124, 20643−20653 Read Online

ACCESS | Metrics & More | Article Recommendations | Supporting Information

ABSTRACT: Inorganic cesium lead halide $CsPbI_xBr_{3-x}$ (x = 0−3) perovskites have recently gained considerable attention as semiconductor materials for the fabrication of photodetectors due to their high thermal and environmental stability. However, preparing high-quality $CsPbI_xBr_{3-x}$ perovskite films using a simple spin-coating method is challenging. This study focused on enhancing the performance of a solution-processed all-inorganic $CsPbI_xBr_{3-x}$ (x = 1, $CsPbIBr_2$) photodetector using a silver iodide (AgI) additive. Introducing a small amount of AgI into the $CsPbIBr_2$ precursor solution resulted in perovskite films that were more uniform and exhibited compact surface morphology that improved crystallinity and electronic properties. To further explore the influence of the AgI-modified $CsPbIBr_2$ perovskite film on the device performance, we fabricated a self-powered photodetector with the geometry of fluorine-doped tin oxide (FTO)/compact TiO_2/$CsI(PbBr_2)_{0.99}(AgI)_{0.01}$/2,2′,7,7′-tetrakis[*N*,*N*-di(4-methoxyphenyl)amino]-9,9′-spirobifluorene (Spiro-OMeTAD)/Au. Photoresponse analysis revealed that the photoresponsivity, on/off ratio, and response time of the $CsI(PbBr_2)_{0.99}(AgI)_{0.01}$ perovskite photodetector were improved. Notably, the $CsI(PbBr_2)_{0.99}(AgI)_{0.01}$ perovskite device showed a higher responsivity and an impressive detectivity of 0.43 A/W and 2.46×10^{11} Jones, respectively, in comparison to the pristine $CsPbIBr_2$ device. This work demonstrates the excellent potential of using inorganic $CsI(PbBr_2)_{0.99}(AgI)_{0.01}$ perovskites in applications for high-performance photodetectors.

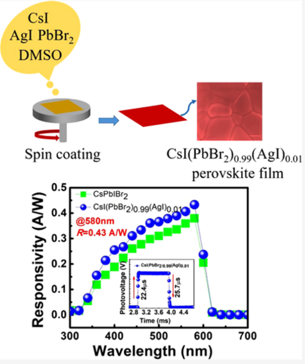

1. INTRODUCTION

Photodetectors (PDs) are essential for imaging, optical communication applications and play crucial roles in various electronic products, such as digital cameras, smartphones, medical diagnostics instruments, biological sensing, remote control, and environmental monitoring.[1,2] Typically, PDs are fabricated as a metal−semiconductor−metal structure, a Schottky junction, or a P−N junction in which the externally applied bias voltage is vital for achieving high sensitivity, high responsivity, and fast detection speed.[3] However, the requirement for external bias adds to both the complexity and operational cost of the PDs. In recent years, self-powered PDs based on n−i−p or p−i−n structures (where n, i, and p refer to the electron transporting layer (ETL), intrinsic layer, and hole transporting layer (HTL), respectively) have gained significant attention since external bias to achieve high-performance photodetection is not required. For self-powered PDs, the performance is strongly influenced by the quality of the intrinsic layer and the ability to separate and transport the photogenerated carriers, i.e., the electron−hole pairs excited by light illumination.[4]

To achieve high-performance self-powered PDs, the intrinsic layer should possess a high absorption extinction coefficient to guarantee sufficient light absorption, high charge carrier mobility, and low defect density for diminishing the dark current density.[5] It is even more attractive if the intrinsic layer can be fabricated using a less complicated method. Solution-processed organic−inorganic perovskites (OIP) have demonstrated excellent optoelectronic properties, which make them promising semiconductor materials for the fabrication of PDs with high sensitivity and fast response speed.[6]

In previous reports, we demonstrated a self-powered PD based on methylammonium lead halide ($MAPbI_3$) with an impressive performance.[7] Recently, we reported on a more robust self-powered triple cation lead halide perovskite ($Cs_{0.05}(FA_{0.83}MA_{0.17})_{0.95}Pb(I_{0.9}Br_{0.1})_3$) using a vertical n−i−p device structure, showing responsivity, detectivity, and on/off ratio of 0.52 A/W, 8.8×10^{12} Jones, and 7.3×10^5. Despite the significant advances in electronic performance, the intrinsic poor thermal and moisture stability issues of OIP hinder their practical applications.[8]

As a promising alternative light-absorbing material, all-inorganic cesium lead halide ($CsPbI_xBr_{3-x}$, x = 0−3) perovskites have shown to be potential candidates for the fabrication of PDs,[4,9,10] due to their superb moisture and

Received: May 8, 2020
Revised: August 3, 2020
Published: August 4, 2020

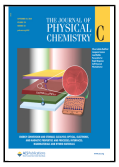

https://dx.doi.org/10.1021/acs.jpcc.0c04144
J. Phys. Chem. C 2020, 124, 20643−20653

thermal stability, as well as the high carrier mobility of all $CsPbI_xBr_{3-x}$ perovskite.[11,12] Xue et al. developed PDs that demonstrated high performance with the responsivity of 0.3 A/W, detectivity of 1.15×10^{13} Jones, and on/off ratio of 4.5×10^2 without bias.[13] Li et al. demonstrated a self-powered perovskite PD based on ZnO nanoparticle-decorated $CsPbBr_3$ films with enhanced photoresponse.[4] Cen et al. later showed a high-performance $CsPbBr_3$ perovskite self-powered PD with an ultralow dark current of 10^{-11} A and a high detectivity of 1.88×10^{13} Jones.[14] The outstanding performance exhibited by the latter report was attributed to the improved $CsPbBr_3$ film quality and interfacial engineering. Also, self-powered PD $CsPbBr_3$ perovskites based on the nanowire and microcrystal structures have been reported with impressive performances.[15,16] However, compared to polycrystalline and single-crystal OIP PDs, the performance parameters of solution-processed $CsPbI_xBr_{3-x}$ perovskite PDs still lag behind. This is primarily due to the high density of trap states and compositional defects in the polycrystalline $CsPbI_xBr_{3-x}$ perovskite film.[17] Therefore, further efforts in the preparation and optimization of $CsPbI_xBr_{3-x}$ PDs are urgently needed. Inorganic $CsPbI_xBr_{3-x}$ perovskite films can be prepared using one-step spin-coating, two-step spin-coating, antisolvent-assisted, and interface engineering strategies.[18] Among these methods, one-step spin coating is still the simplest and less complicated method. However, the one-step spin-coating method usually results in relatively low-quality $CsPbI_xBr_{3-x}$ perovskite films with a large number of grain boundaries and compositional defects that can easily cause charge recombination in grain boundaries of the resulting devices.[19] Li et al. have proven that low-quality $CsPbX_3$ perovskite films can easily be mixed with the upper HTL such as 2,2′,7,7′-tetrakis[*N*,*N*-di(4-96 methoxyphenyl)amino]-9,9′-spirobifluorene (Spiro-OMe97 TAD), which can further cause charge recombination in another way.[18,20]

Among the all-inorganic $CsPbI_xBr_{3-x}$ perovskite system, the $CsPbI_xBr_{3-x}$ (where $x = 1$, $CsPbIBr_2$) is the most promising candidate for optoelectronic device applications (e.g., solar cells and PDs) due to its stable α-phase and suitable band gap of about 2.05 eV.[19] Recently, Bao et al. found that through the optimization of the film quality and device engineering, $CsPbIBr_2$-based perovskite PDs can achieve high sensitivity and fast response speed.[1] Although Bao et al. have shown a novel approach to boost the figure of merit of $CsPbIBr_2$ perovskite-based PDs and their potential for optical and communication applications, a simple and attractive method to improve the electronic quality of the solution-processed polycrystalline $CsPbIBr_2$ perovskite films for high-performance self-powered PDs is needed. Moreover, the incorporation of the all-inorganic perovskite film that possesses high crystallinity, uniform surface coverage, and fewer defects into self-powered PDs is a great advancement for the next generation of photodetection.

In this work, we report on one-step spin coating and an additive-assisted solution-processed $CsPbIBr_2$ perovskite film for the fabrication of a self-powered PD. Herein, for the first time, we incorporated a silver iodide (AgI) additive into the $CsPbIBr_2$ perovskite precursor to form the $CsI(PbBr_2)_{0.99}(AgI)_{0.01}$ composition. The $CsI(PbBr_2)_{0.99}(AgI)_{0.01}$ perovskite clearly exhibits several advantages of uniform coverage, phase pure, enlarge grain size, higher crystallinity, fewer defects perovskite films. A self-powered PD based on $CsI(PbBr_2)_{0.99}(AgI)_{0.01}$ perovskite was fabricated. The device showed improvement in the performance parameters such as higher photocurrent, lower dark current, higher on/off ratio, better photoresponsivity, and faster response speed in comparison to the pristine $CsPbIBr_2$ perovskite device. Notably, the responsivity and response speed of the $CsI(PbBr_2)_{0.99}(AgI)_{0.01}$ perovskite PD are much higher than most previously reported self-powered all-inorganic $CsPbI_xBr_{3-x}$ PDs. This work offers an effective strategy for improving the film quality of $CsPbIBr_2$ perovskites for the fabrication of high-performance perovskite-based PDs.

2. EXPERIMENTAL SECTION

2.1. Materials and Reagent. Lead bromide ($PbBr_2$, 99.0%), cesium iodide (CsI, 99.0%), and silver iodide (AgI, 99.999%) were purchased from Sigma-Aldrich. Fluorine-doped tin oxide (FTO) glass substrates (sheet resistance: 12−15 Ω/sq) were purchased from MSE supplies. Liquid detergent (Hellmanex), acetone, isopropanol, ethanol, chlorobenzene, and titanium(IV) chloride ($TiCl_4$, Alfa Aesar), and dimethyl sulfoxide (DMSO; 99.0%, Sigma-Aldrich). Spiro-OMeTAD (99.0%, Sigma- Aldrich), lithium bis(trifluoromethane)-sulfonimide (Li-TFSI, 99.0%, Sigma-Aldrich), and 4-*tert*-butylpyridine (TBP, 99.0%, Sigma-Aldrich).

2.2. Device Fabrication. FTO-coated glass substrates were patterned by etching with hydrochloric acid (HCl) and zinc (Zn) powder and sequentially cleaned with Hellmanex, nanopure water, acetone, and isopropanol. The substrates were then treated with an oxygen plasma cleaner for 5 min. The compact TiO_2 (c-TiO_2) ETL was prepared as reported elsewhere[21] and spin-coated at 3000 rpm for 30 s and dried at 125 °C for 10 min. The c-TiO_2 layer was further subjected to chemical bath treatment using $TiCl_4$ (0.04 M) at 70 °C for 30 min. The films were subsequently annealed at 500 °C for 30 min.[21,22] The inorganic $CsPbIBr_2$ perovskite layer was prepared using a one-step solution process method. First, the $CsPbIBr_2$ precursor solutions were prepared in a nitrogen-filled glovebox by mixing CsI (1 M) and $PbBr_2$ (1 M) in DMSO (1 mL). The precursor solution containing the AgI additive was prepared by introducing 1% mass percentage of AgI with respect to $PbBr_2$ into the solution. The precursor solutions were stirred for 12 h at 70 °C. Next, the perovskite films were prepared by drop casting the solution on top of the c-TiO_2 layer and spin-coated at 1500 rpm for 45 s to obtain a thickness of about 250 nm. Finally, the perovskite films were thermally annealed at 70 °C for 2 min, followed by 280 °C for 10 min. The HTL was prepared by spin coating a solution of Spiro-OMeTAD on top of the perovskite film at a spin speed of 2000 rpm for 60 s. The obtained Spiro-OMeTAD thickness was ~230 nm. The Spiro-OMeTAD solution was prepared by mixing 17.5 μL of Li-TFSI solution (520 mg of Li-TSFI in 1 mL of acetonitrile), 28.8 μL of TBP with 90 mg of Spiro-OMeTAD in 1 mL of chlorobenzene solution. The final devices were completed by thermal evaporation of Au back contacts with a thickness of 100 nm at 3.4×10^{-4} Pa. The active area of the devices was 0.06 cm^2.

2.3. Materials and Device Characterization. The crystalline structures of the perovskite films were characterized by powder X-ray diffraction (XRD) (Scintag Pad-V XRD powder diffractometer, graphite monochromated Cu Kα radiation). The absorption spectra were collected using an Agilent Cary 5000. External quantum efficiency (EQE) measurements were performed using light from the 300 W xenon lamp passed through a cornerstone 260 monochromator

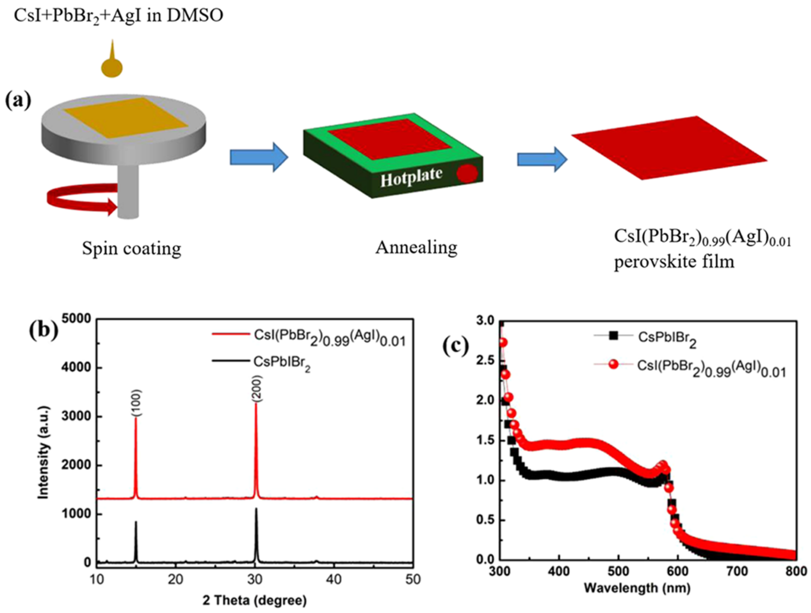

Figure 1. Processing procedures for the fabrication of the $CsI(PbBr_2)_{0.99}(AgI)_{0.01}$ perovskite film. (b) XRD patterns of the $CsPbIBr_2$ and $CsI(PbBr_2)_{0.99}(AgI)_{0.01}$ perovskite films. (c) UV−vis absorption spectra of the $CsPbIBr_2$ and $CsI(PbBr_2)_{0.99}(AgI)_{0.01}$ perovskite films.

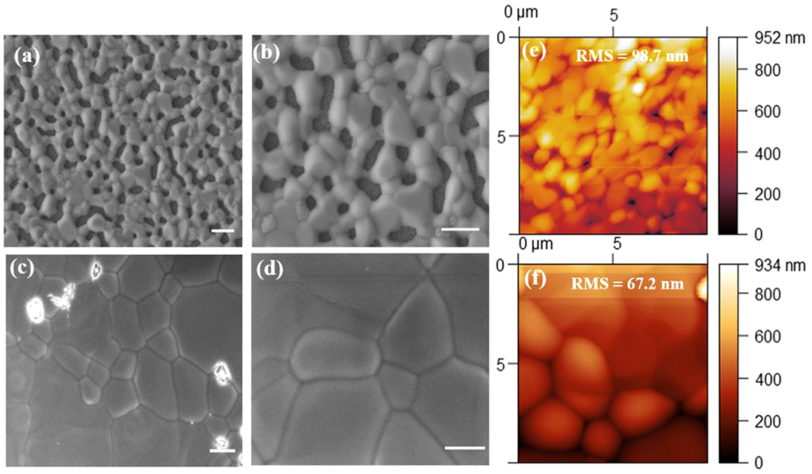

Figure 2. Comparison of the high- and low-magnification SEM of (a, b) $CsPbIBr_2$ and (c, d) $CsI(PbBr_2)_{0.99}(AgI)_{0.01}$ perovskite films and the AFM images of the $CsPbIBr_2$ perovskite film (e), $CsI(PbBr_2)_{0.99}(AgI)_{0.01}$ perovskite film (f). The scale bar for the SEM images is 2 μm.

(Newport, 74125) onto the cells and the light scanned from 300 to 700 nm in 5 nm intervals. Incident-light intensity and photocurrent were measured using a power meter (Newport, 2936-C) and an Oriel 71580 silicon detector head (Newport). Steady-state photoluminescence (PL) data were collected at room temperature using an Edinburgh instruments FS5 spectrometer. The samples were excited by a picosecond pulsed light-emitting diode (EPLED-365 nm). The time-resolved photoluminescence (TRPL) was measured using the time-correlated single-photon counter, excited by a picosecond pulsed diode laser (EPL-450 nm). Scanning electron microscopy (SEM) images and energy-dispersive X-ray spectroscopy (EDS) were performed by a high-resolution field emission scanning electron microscope (FESEM, JEOL 7401F). Atomic force microscopy (AFM) images were obtained using a Bruker Icon scanning probe microscope (SPM). The current density−voltage (*J*−*V*) measurements were obtained by a Keithley 2400 integrated with LabView under a white light light-emitting diode (LED) lamp with an intensity of 100 mW/cm^2. The photovoltage−time measurements were obtained using a NI-6210 data acquisition device (DAQ). The signal from the DAQ (NI-6210) to the computer was boosted with the Hamamatsu C7319 on low bandwidth setting and 10^5 gain and powered with an Agilent E3630A at 6 V. MATLAB was used to collect and process the data. The light source was powered by a GwInstek GFG-8255A function generator, creating a square wave with an amplitude of 2 V to power a 470 nm LED. The electrochemical impedance spectra (EIS) (Gamry Instruments, Interface 1000) were performed scanning from 10^6 to 0.02 Hz.[23,24] The measurements were performed at open-circuit voltage under 1 sunlight illumination. The Nyquist plots were fit by using the Gamry Echem Analyst software using the equivalent circuit, as shown in Figure 8c.

3. RESULTS AND DISCUSSION

Figure 1a presents the fabrication method of the $CsI(PbBr_2)_{0.99}(AgI)_{0.01}$ perovskite film using a one-step spin-

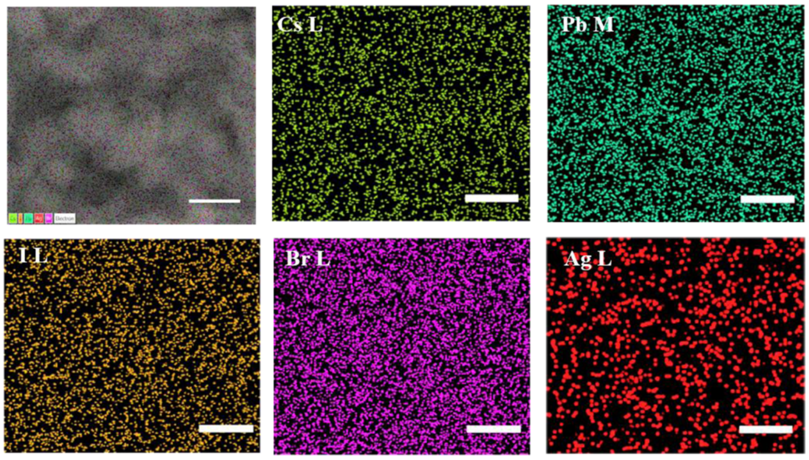

Figure 3. EDS elemental mapping images of Cs, Pb, I, Br, and Ag elements for the $CsI(PbBr_2)_{0.99}(AgI)_{0.01}$ perovskite film. The scale bar is 1 μm.

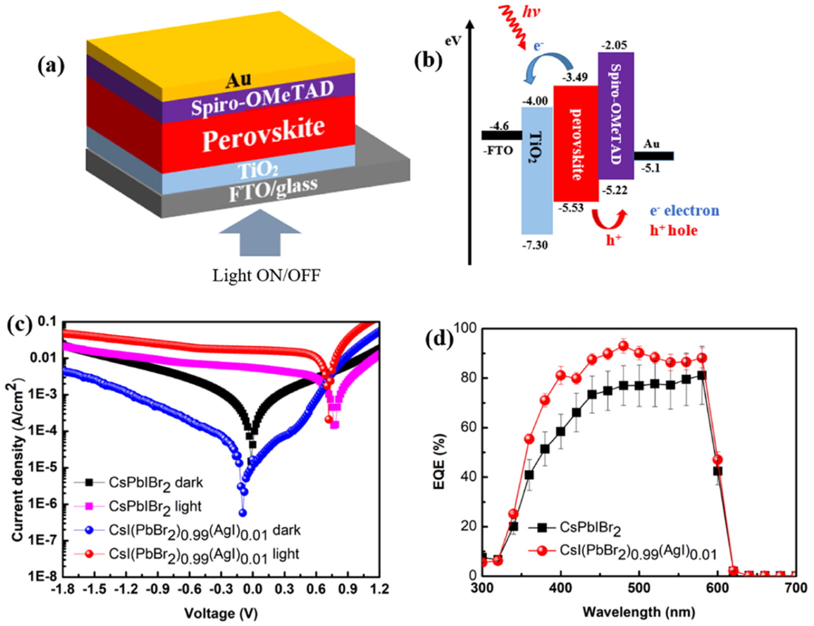

Figure 4. (a) Schematic diagram of the device structure. (b) Energy level diagram, (c) $J-V$ curves of the devices in the dark and under white light illumination (100 mW/cm^2), and (d) EQE of the $CsPbIBr_2$ and $CsI(PbBr_2)_{0.99}(AgI)_{0.01}$ perovskite PDs under 0 V bias with corresponding error bars.

coating process. The $CsI(PbBr_2)_{0.99}(AgI)_{0.01}$ perovskite precursor solution was prepared by partial substitution of $PbBr_2$ with 1% AgI (mass percent), which is in accordance with previously reported work.[25] Shahbazi et al. had previously reported a simple synthetic approach to grow uniform $CH_3NH_3PbI_3$ perovskite layers free of pin holes via a varied portion of AgI added to the precursor solution. Their studies confirmed that both 1% AgI was the optimum doping level for device fabrication. Following their pioneering work, we prepared a $CsPbIBr_2$ perovskite film with 1% AgI, which we compared with the pristine $CsPbIBr_2$ perovskite film.[25] The precursor solution was one-step deposited on top of the FTO/c-TiO_2 layer to form the $CsI(PbBr_2)_{0.99}(AgI)_{0.01}$ perovskite film. Detailed preparation procedures can be found in Section 2. XRD measurements were conducted to investigate the crystal structure of the $CsI(PbBr_2)_{0.99}(AgI)_{0.01}$ and $CsPbIBr_2$ perovskite films. Figure 1b shows the XRD patterns of the $CsPbIBr_2$ and $CsI(PbBr_2)_{0.99}(AgI)_{0.01}$ perovskite films. The main diffraction peaks around 14.93 and 30.16° can be assigned to the lattice plane (100) and (200) of the α-phase perovskite,[26,27] respectively. The perovskite thin films showed no characteristics peaks for Ag because the amount in the bulk of the $CsI(PbBr_2)_{0.99}(AgI)_{0.01}$ perovskite was too small to show their diffraction peaks.[28,29] By comparison, the diffraction peak intensities of the (100) and (200) crystal planes were stronger for the $CsI(PbBr_2)_{0.99}(AgI)_{0.01}$ perovskite film, indicating better crystallinity with fewer grain defects. Figure 1c shows the UV−vis absorption spectra of the $CsPbIBr_2$ and $CsI(PbBr_2)_{0.99}(AgI)_{0.01}$ perovskite films. The $CsI(PbBr_2)_{0.99}(AgI)_{0.01}$ perovskite film showed improved absorption, which is probably related to its higher crystallinity and/or improved surface morphology (as discussed hereafter). The band gap of both perovskite films was estimated to be 2.06 and 2.07 eV for the $CsPbIBr_2$ and $CsI(PbBr_2)_{0.99}(AgI)_{0.01}$ perovskite films, respectively, using the Tauc plot (Figure S1), which is consistent with the previously reported values.[30] Interestingly, the band gap of the pristine $CsPbIBr_2$ appeared to be unchanged when modified with the 1% AgI additive. Figure 2

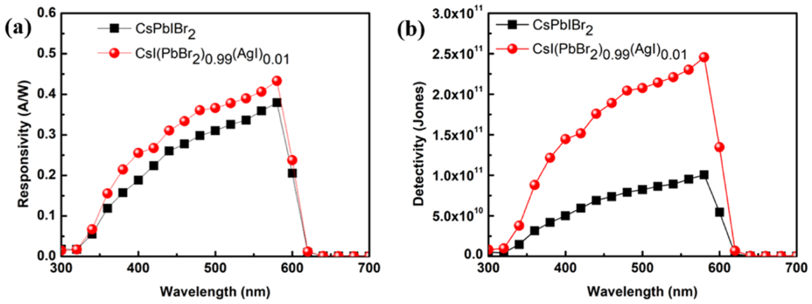

Figure 5. (a) Responsivity and (b) detectivity of the $CsPbIBr_2$ and $CsI(PbBr_2)_{0.99}(AgI)_{0.01}$ perovskite PDs, respectively, under 0 V bias.

shows the low and high magnification of the SEM images of the $CsPbIBr_2$ and $CsI(PbBr_2)_{0.99}(AgI)_{0.01}$ perovskite films. As shown in Figure 2a,b, the $CsPbIBr_2$ perovskite film exhibited a nonuniform morphology with a void on its surface. Previously reported work has suggested that the formation of such voids is probably due to the extremely slow crystallization of $CsPbIBr_2$, where $CsPbIBr_2$ species will crystallize from the precursor film containing plenty of DMSO molecules and then shrink to leave isolated voids behind.[19] The $CsI(PbBr_2)_{0.99}(AgI)_{0.01}$ perovskite film showed marked changes in the surface morphology (Figure 2c,d). A compact and uniform morphology with larger grain sizes and fewer grain boundaries can be observed. These features are expected to lower crystal defects and trap densities, while also act to reduce charge recombination as well as enhancing charge transport in the device.[21,22,31−34] Figure S2 shows the possible underlying mechanism of the improved surface coverage for the $CsI(PbBr_2)_{0.99}(AgI)_{0.01}$ perovskite film. Upon spin coating of the precursor solution containing the AgI additive, Ag islands were formed, which could act as the nucleation promoter for the perovskite to grow and merge into a continuous film with less grain boundaries and enhanced crystallinity.[35−37]

We also compared the AFM images of the $CsPbIBr_2$ and $CsI(PbBr_2)_{0.99}(AgI)_{0.01}$ perovskite films, as shown in Figure 2e,f. The root-mean-square (RMS) roughness values were estimated to be 98.7 and 67.2 nm for the $CsPbIBr_2$ and $CsI(PbBr_2)_{0.99}(AgI)_{0.01}$ perovskite films, respectively. The lower RMS value for the $CsI(PbBr_2)_{0.99}(AgI)_{0.01}$ perovskite film confirms the presence of additive AgI and that it can passivate the surficial morphology of the perovskite film. Also, the reduced surface roughness would produce fewer defects and traps in the interface between $CsI(PbBr_2)_{0.99}(AgI)_{0.01}$ and Spiro-OMeTAD layers, resulting in efficient charge extraction.[38−41]

EDS elemental mapping was conducted to confirm that Ag ions coexisted with the $CsI(PbBr_2)_{0.99}(AgI)_{0.01}$ perovskite film. Figure 3 shows the elemental mapping images for the $CsI(PbBr_2)_{0.99}(AgI)_{0.01}$ perovskite film. The Ag element was detected and evenly distributed in the perovskite film, indicating the successful incorporation of Ag into the bulk of the perovskite film. The uniform distribution of Ag inside the $CsI(PbBr_2)_{0.99}(AgI)_{0.01}$ perovskite film provides a strong indication to show that AgI was dissolved inside the perovskite lattice and did not form the AgI agglomerations or other Ag-rich phases.[25]

Furthermore, we applied the $CsI(PbBr_2)_{0.99}(AgI)_{0.01}$ perovskite to fabricate a self-powered PD with a geometry of FTO/c-TiO_2/$CsI(PbBr_2)_{0.99}(AgI)_{0.01}$/Spiro-OMeTAD/Au, as shown in Figure 4a. The performance of the device based on the $CsI(PbBr_2)_{0.99}(AgI)_{0.01}$ perovskite film was compared with the device constructed using the pristine $CsPbIBr_2$ perovskite film. Figure 4b shows the energy diagram of the self-powered PD, with its energy values extracted from the literature.[42,43] Typically, when the perovskite absorbs photon energies larger than its band gap, the layer can generate quasi-free carriers and electron−hole pairs that swiftly dissociate at the TiO_2/perovskite and perovskite/Spiro-OMeTAD interfaces (see Figure 4b). Subsequently, these electrons and holes were collected by the anode and cathode, respectively, generating a photocurrent in the device. A higher photocurrent and lower dark current can be achieved in vertical structure PD at 0 V if the perovskite layer is of high quality, i.e., with fewer crystal defects, uniform, and pinhole-free morphology with smaller grain boundaries and so on. Figure 4c shows the $J-V$ curves of the $CsPbIBr_2$ and $CsI(PbBr_2)_{0.99}(AgI)_{0.01}$ PDs measured in the dark and under LED white light illumination (100 mW/cm^2). The $CsI(PbBr_2)_{0.99}(AgI)_{0.01}$ perovskite device exhibited a dark current of 9.71×10^{-6} A/cm^2 under 0 V, which was lower than the dark current of the $CsPbIBr_2$ device (4.44×10^{-5} A/cm^2). To further substantiate the lower dark current density exhibited by the $CsI(PbBr_2)_{0.99}(AgI)_{0.01}$ perovskite PDs, the dark current densities of 8 devices were tested under the same conditions and statistically analyzed, as shown in Figure S3. In comparison, it is apparent that the dark current densities of $CsI(PbBr_2)_{0.99}(AgI)_{0.01}$ are lower with a lesser scattering of the statistical plot, suggesting that the $CsI(PbBr_2)_{0.99}(AgI)_{0.01}$ perovskite film possesses higher quality with lower trap density and recombination rates. Furthermore, the light on/off ratios were determined to be 1.68×10^3 and 1.21×10^2 for $CsI(PbBr_2)_{0.99}(AgI)_{0.01}$ and $CsPbIBr_2$ perovskite PDs, respectively. Notably, the on/off ratio of the $CsI(PbBr_2)_{0.99}(AgI)_{0.01}$ perovskite device was higher than the pristine device by one order of magnitude. The lower dark current and higher on/off ratio exhibited by the $CsI(PbBr_2)_{0.99}(AgI)_{0.01}$ perovskite-based PD can be attributed to the improved film quality. We further assessed the performance of the self-powered PDs using the EQE measurements. The EQE is a measure of the number of photogenerated carriers that an incident photon at a given wavelength produces per second and can be estimated using the expression below.

$$\mathrm{EQE} = \frac{J_{ph} h\nu}{P_{in} e} = \frac{(J_{light} - J_{dark}) h\nu}{P_{in} e} \qquad (1)$$

where J_{ph} is the photocurrent density, P_{in} is the incident intensity, e is the elementary charge, J_{dark} is the dark current density, and J_{light} is the current density under illumination. Figure 4d shows the EQE spectra of $CsPbIBr_2$ and $CsI(PbBr_2)_{0.99}(AgI)_{0.01}$ perovskite-based PDs at 0 V bias with corresponding error bars. The $CsI(PbBr_2)_{0.99}(AgI)_{0.01}$ perov-

https://dx.doi.org/10.1021/acs.jpcc.0c04144
J. Phys. Chem. C 2020, 124, 20643−20653

Table 1. Summary of the Performance Parameters for the Self-Powered $CsPbI_xBr_{3-x}$ PD Devices

device structure	dark current@0 V bias (A/cm^2)	responsivity (A/W)	detectivity (Jones)	τ_{rise}/τ_{rise}	ref
$FTO/TiO_2/CsI(PbBr_2)_{0.99}(AgI)_{0.01}$/Spiro-OMETAD/Au	9.71×10^{-6}	0.43	2.46×10^{11}	22.4/25.7 μs	this work
$FTO/TiO_2/CsPbIBr_2$/Spiro-OMeTAD/Au	4.44×10^{-5}	0.38	1.00×10^{11}	43.7/47.2 μs	this work
$FTO/TiO_2/CsPbBr_3$/carbon	8.05×10^{-11}	0.35	3.83×10^{13}	−/1.46 μs	56
$FTO/CsPbBr_3$:ZnO/Ag	0.240	0.0115		0.41/0.018s	4
$FTO/ZnO/CsPbBr_3/MoO_3$/Au		0.3	1.15×10^{13}	200/500 ms	13
$FTO/Al_2O_3/CsPbBr_3/TiO_2$/Au	10 nA	0.44	1.88×10^{13}	28/270 μs	14
$Au/CsPBr_3$/Pt	10 pA	0.028	1.7×10^{11}	230/60 ms	57
$Ag/CsPbBr_3$/CuI/Ag		0.0014	6.2×10^{10}	0.04/2.96 ms	58
$ITO/SnO_2/CsPbBr_3$/Spiro-OMeTAD/Au	<10 nA	0.172	4.8×10^{12}	0.14/0.12 ms	16
$ITO/SnO_2/CsPbBr_3$/PTAA/Au	2.5×10^{-9}	0.206	7.23×10^{12}	30/39 μs	59
$GaN/CsPbBr_3$/ZnO	1×10^{-9}	0.0895	1.03×10^{14}	100/140 μs	60
$ITO/SnO_2/PMMA/CsPbBr_3$/PTAA/Au	4.0×10^{-9}	0.3	1.0×10^{13}	0.4/0.43 ms	15

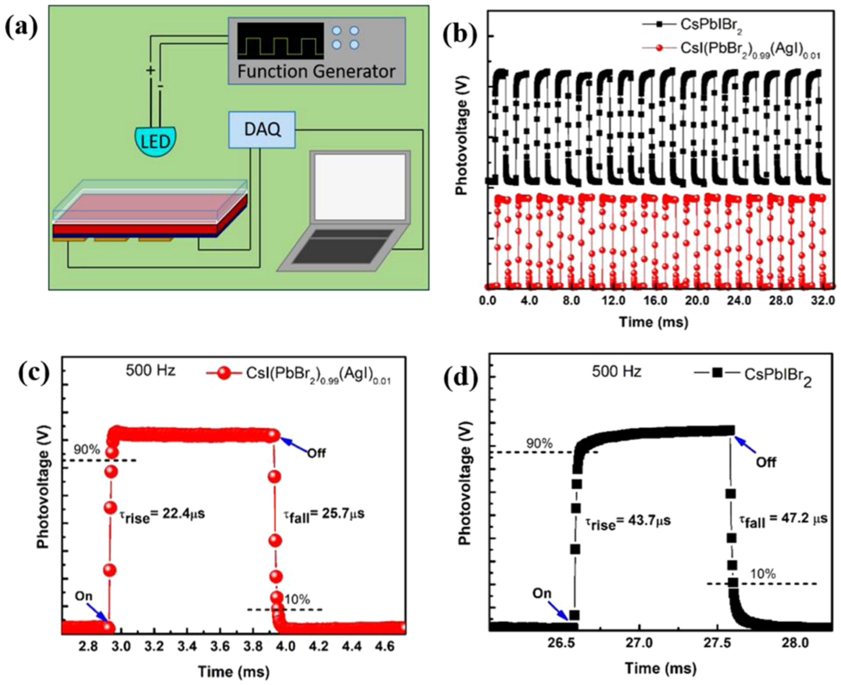

Figure 6. (a) Illustration of the setup for response time measurement. The DAQ used was NI-6210 controlled by an in-house MATLAB program. (b) On−off cycles of the $CsPbIBr_2$ and $CsI(PbBr_2)_{0.99}(AgI)_{0.01}$ PD under a 470 nm pulse light from an LED at a frequency of 500 Hz, (c) corresponding rise and decay time of the $CsPbIBr_2$ perovskite PD, and (d) corresponding rise and decay time of the $CsI(PbBr_2)_{0.99}(AgI)_{0.01}$ perovskite PD.

skite PD showed higher EQE from 320 to 580 nm compared to the $CsPbIBr_2$-based device, suggesting that the charge carriers are efficiently extracted to their respective electrodes. In contrast, from Figure 4d it is also apparent that the $CsI(PbBr_2)_{0.99}(AgI)_{0.01}$ perovskite PD has lower variability of errors in the device measurements, which further corroborates the beneficial effect of the improved $CsI(PbBr_2)_{0.99}(AgI)_{0.01}$ perovskite film quality.

The responsivity (R) spectra and detectivity (D^*) curves of $CsPbIBr_2$- and $CsI(PbBr_2)_{0.99}(AgI)_{0.01}$-based perovskite PDs were calculated and are provided in Figure 5a,b. R is the measure of electrical output per watt of incident radiant power, which can be expressed using the below equation2[44]

$$R = \frac{J_{ph}}{P_{in}} = \frac{EQE \times \lambda e}{hc} \tag{2}$$

where λ is the incident-light wavelength, h is the Planck constant, and c is the speed of light. The D^* represents the device's capability of detecting low-level light signals and is calculated using the below equation3[44,45]

$$D^* = \frac{R}{\sqrt{2qJ_{dark}}} \tag{3}$$

Equation 3 provides an approximate expression of the specific detectivity when shot noise is the dominant noise in the system. Therefore, the calculation provides an upper estimate of the actual specific detectivity. The R of 0.43 A/W was apparently achieved, which is higher than the most previously report as summarized in Table 1 below, and D^* of 2.46×10^{11} Jones for the $CsI(PbBr_2)_{0.99}(AgI)_{0.01}$ perovskite PD is higher than the control device (see Figure 5a,b). The higher R and D^* values exhibited by the device are a further indication that the $CsI(PbBr_2)_{0.99}(AgI)_{0.01}$ perovskite film was

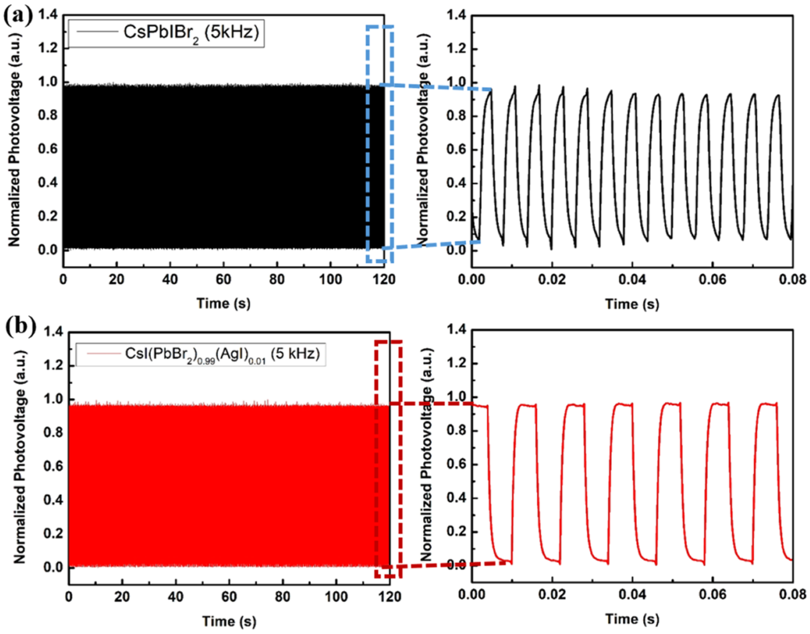

Figure 7. Response of the PDs based on (a) $CsPbIBr_2$, (b) $CsI(PbBr_2)_{0.99}(AgI)_{0.01}$ at 0 V bias under a 470 nm on/off modulated light from an LED in a test period of about 120 s measured in ambient condition. The right panels for $CsPbIBr_2$ and $CsI(PbBr_2)_{0.99}(AgI)_{0.01}$ show the enlarged detail of the response.

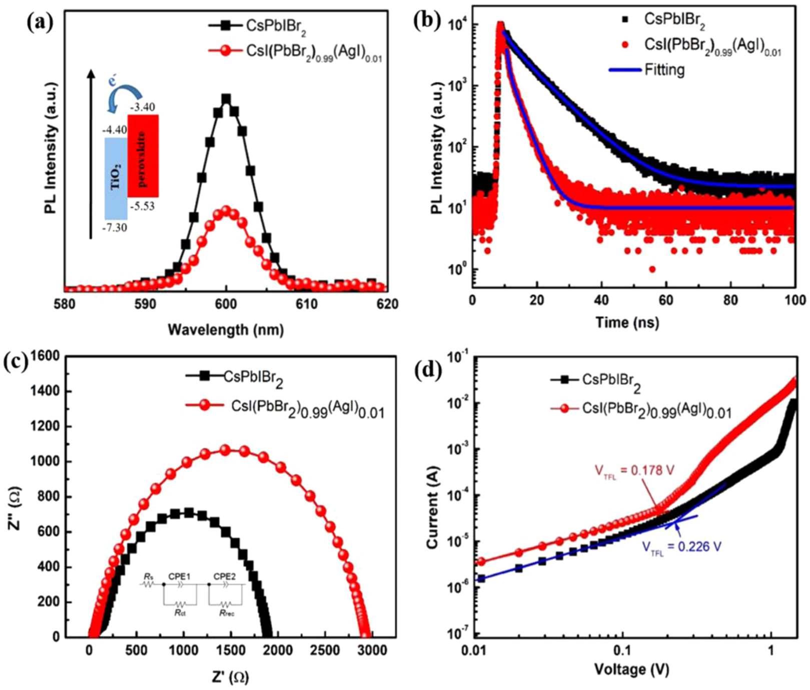

Figure 8. (a) Steady-state PL spectra (the inset schematically represents the charge transfer at the perovskite/TiO_2 interface), (b) TRPL spectra of the corresponding perovskite films on the FTO/c-TiO_2 substrates, (c) Nyquist plot of the $CsPbIBr_2$- and $CsI(PbBr_2)_{0.99}(AgI)_{0.01}$-doped perovskite solar cells (PSCs) recorded under 1 sun illumination. The inset is the simulated equivalent circuit, where R_s, R_{ct}, R_{rec}, CPE_1, and CPE_2 are the series resistance of the electrode, charge-transfer resistance, the recombination resistance, space charge capacitance or ionic capacitance, and chemical capacitance, respectively. Dark $I-V$ curves of electron only devices (FTO/c-TiO_2/perovskite/phenyl-C_{61}-butyric acid methyl ester (PCBM)/Ag) for (d) $CsPbIBr_2$ and $CsI(PbBr_2)_{0.99}(AgI)_{0.01}$ perovskite films.

of high crystalline quality with fewer defects, resulting in efficient photon absorption, charge generation, and transport to the electrode.

The response speed is another crucial parameter for PDs, which reveals its capability to follow a fast-varying optical signal. Fast and reproducible responses to light illumination are important for high-performance PDs for application in smart systems, image sensing, structural health monitoring, and optical communication.[1,46−51] Figure 6a presents the illustration of the setup for response time measurement. The response time of the $CsI(PbBr_2)_{0.99}(AgI)_{0.01}$ perovskite PD was measured using a 470 nm pulse light source from an LED and driven by a function generator with square waves at a frequency of 500 Hz under ambient condition. Both devices clearly exhibited stable and reproducible transient responses (Figure 6b), suggesting that both $CsPbIBr_2$ and $CsI(PbBr_2)_{0.99}(AgI)_{0.01}$ are excellent candidates for the fabrication of PDs. We further analyzed the rise (τ_{rise}) and fall (τ_{fall}) time of both devices, which were the time taken for the PD to reach 90% and drop to 10% of the steady-state values, respectively, as shown in Figure 6c,d. The $CsPbIBr_2$ device shows a τ_{rise} and τ_{fall} of 43.7 and 47.2 μs, respectively, while the $CsI(PbBr_2)_{0.99}(AgI)_{0.01}$ perovskite PD showed a dramatic faster τ_{rise} and τ_{fall} of 22.4 and 25.7 μs, respectively.

The response speed of the $CsI(PbBr_2)_{0.99}(AgI)_{0.01}$ perovskite self-powered PD was higher than most of the previously reported work, as summarized in Table 1. We further studied the repeatability of the transient response of the PDs at a pulse frequency of 5 kHz for a period of 120 s. Figure 7a,b shows the transient response of PDs based on the $CsPbIBr_2$ and $CsI(PbBr_2)_{0.99}(AgI)_{0.01}$ perovskites under a 470 nm pulse light from an LED at 5 kHz. Both PDs demonstrated reproducible and repeatable transient responses, suggesting that $CsPbIBr_2$ and $CsI(PbBr_2)_{0.99}(AgI)_{0.01}$ perovskites are reliable and superb materials for high-speed optical applications. Notably, the enlarged details of the transient response for the $CsPbIBr_2$ and $CsI(PbBr_2)_{0.99}(AgI)_{0.01}$ perovskite PDs revealed that the rise/fall of the transient signal of the $CsI(PbBr_2)_{0.99}(AgI)_{0.01}$ perovskite PD was faster and also retained the square light pulse, as shown in Figure 6b−d. This further substantiates that the $CsI(PbBr_2)_{0.99}(AgI)_{0.01}$ perovskite PD had fewer defects and charge recombination.

To understand the mechanism of the photoelectrical response enhancement observed for the $CsI(PbBr_2)_{0.99}(AgI)_{0.01}$ PD, the steady-state PL measurements were performed on the $CsPbIBr_2$ and $CsI(PbBr_2)_{0.99}(AgI)_{0.01}$ perovskite films deposited on top of TiO_2 ETL (Figure 8a). Both perovskite films showed a peak at ∼600 nm, which is consistent with the band gap of $CsPbIBr_2$. Notably, the maximal PL intensity for the $CsI(PbBr_2)_{0.99}(AgI)_{0.01}/TiO_2$ film was quenched by nearly 60% with respect to the PL intensity of the pristine $CsPbIBr_2$ film. Such a dramatic quenching is attributed to the high-quality perovskite layer, which induced an efficient charge transfer at the interface and exciton dissociation,[52−55] as schematically shown in the inset of Figure 8a. Furthermore, the emission dynamics of the $CsPbIBr_2$ and $CsI(PbBr_2)_{0.99}(AgI)_{0.01}$ perovskite films was studied using the TRPL (Figure 8b). The TRPL decay curves were fitted using the biexponential decay function shown in the following equation

$$y = A_1 \exp\left(\frac{-t}{\tau_1}\right) + A_2 \exp\left(\frac{-t}{\tau_2}\right) + y_0 \tag{4}$$

where A_1 and A_2 are the time-independent coefficients of the amplitude fraction, τ_1 represents the fast decay component, and τ_2 is the slow decay component. τ_1 can be ascribed to the interface recombination and τ_2 is related to the recombination process in the bulk of the perovskite layer.[61] The results of the TRPL also correspond to the steady-state PL, which reveals a much faster PL decay for the $CsI(PbBr_2)_{0.99}(AgI)_{0.01}$ perovskite film with the values of τ_1 of 0.39 ns and τ_2 of 2.13 ns, which was shorter than those of the pristine $CsPbIBr_2$ perovskite film with τ_1 of 2.05 ns and τ_2 of 5.77 ns. The smaller τ_1 suggests less trap charge recombination and faster carrier extraction efficiency at the interface due to the improvement of the perovskite film quality.

EIS measurements were employed to further investigate the interfacial charge transport and recombination dynamics of the $CsPbIBr_2$ and $CsI(PbBr_2)_{0.99}(AgI)_{0.01}$ perovskite PDs. Figure 8c presents the EIS spectra of the $CsPbIBr_2$ and $CsI(PbBr_2)_{0.99}(AgI)_{0.01}$ PDs. The measurements were performed from 1 MHz to 0.02 Hz under 1 sunlight illumination (AM 1.5) at an applied open-circuit voltage. The inset is the adopted equivalent circuit for the Nyquist plot fitting. In the equivalent circuit, the R_s, R_{ct}, R_{rec}, CPE_1, and CPE_2 represent the series resistance of the electrode, charge-transfer resistance, the recombination resistance, space charge capacitance or ionic capacitance, and chemical capacitance, respectively. From the Nyquist plots, the relatively small arc at a high frequency is related to the hole-transport process at the Spiro-OMeTAD (HTL)/perovskite interface, corresponding to a charge-transfer resistance (R_{ct}) in parallel with the hole-transport material (HTM) capacitance (CPE_1).[62] The large arc at the low frequency is due to recombination at the TiO_2 ETL/perovskite interface, which can be expressed by R_{rec} in parallel with the CPE_2. Table S1 presents the summary of the EIS spectra parameters analyzed with fitting the Nyquist plots. The R_{ct} decreased from 115.5 to 43.28 Ω for the $CsPbIBr_2$ and $CsI(PbBr_2)_{0.99}(AgI)_{0.01}$ perovskite PDs, respectively. The decreased R_{ct} suggests a more effective charge extraction and collection process in the $CsI(PbBr_2)_{0.99}(AgI)_{0.01}$ perovskite device, leading to an enhanced photoresponsivity.[63,64] The R_{rec} of the $CsI(PbBr_2)_{0.99}(AgI)_{0.01}$ perovskite device is 2613 Ω, which is higher than that of the pristine $CsPbIBr_2$ perovskite device (1740 Ω), indicative of a decreased carrier recombination between the TiO_2 ETL/$CsI(PbBr_2)_{0.99}(AgI)_{0.01}$ perovskite.[18,27,63] The R_s value for the $CsI(PbBr_2)_{0.99}(AgI)_{0.01}$ perovskite device was lower than the pristine $CsPbIBr_2$ perovskite device, further suggesting that the $CsI(PbBr_2)_{0.99}(AgI)_{0.01}$ perovskite device has decreased leakage current and is beneficial to obtaining a lower dark current density.

To determine the trap state density (n_{trap}), electron only devices with a geometry of FTO/c-TiO_2/perovskite/PCBM/Ag were fabricated. Figure 8d shows the plots of $I-V$ curves under dark conditions. The trap state density can be determined from the trap-filled limit voltage (V_{TFL}), according to the equation below.[65,66]

$$n_{trap} = \frac{2\varepsilon\varepsilon_0}{ed^2} V_{TFL} \tag{5}$$

where ε is the relative dielectric constant of $CsPbIBr_2$, which is approximately equal to 8,[18,67] ε_0 is the constant of vacuum permittivity in free space, d is the thickness of the perovskite film, and e is the electron charge. V_{TFL} is estimated from the $I-V$ curves. Table S2 shows the V_{TFL} and n_{trap} values of the $CsPbIBr_2$ and $CsI(PbBr_2)_{0.99}(AgI)_{0.01}$ perovskite PDs. The approximate V_{TFL} values for the $CsPbIBr_2$ and $CsI(PbBr_2)_{0.99}(AgI)_{0.01}$ perovskite devices are 0.226 and 0.178 V, respectively. The n_{trap} for the device $CsPbIBr_2$ and $CsI(PbBr_2)_{0.99}(AgI)_{0.01}$ perovskite films are calculated to be 3.20×10^{15} and 2.52×10^{15} cm^{-3}, respectively. The defect density for the $CsI(PbBr_2)_{0.99}(AgI)_{0.01}$ perovskite device was reduced in comparison to the $CsPbIBr_2$ perovskite device. The decrease in defect density for the $CsI(PbBr_2)_{0.99}(AgI)_{0.01}$ perovskite device can be attributed to the high-quality perovskite film with higher crystallinity, enlarging grains, and fewer grain boundaries and defects.

4. CONCLUSIONS

In summary, we prepared all-inorganic $CsI(PbBr_2)_{0.99}(AgI)_{0.01}$ perovskite polycrystalline films by a simple solution-processed method for the fabrication of a self-powered PD. The novel $CsI(PbBr_2)_{0.99}(AgI)_{0.01}$ perovskite film possessed uniform surface morphology, a pure phase, microsized grains, higher crystallinity, and fewer defects in contrast with the pristine $CsPbIBr_2$ perovskite film. The resulting self-powered PD with a simple architecture of FTO/c-TiO_2/$CsI(PbBr_2)_{0.99}(AgI)_{0.01}$/Spiro-OMeTAD/Au had a lower dark current density of 9.71×10^{-6} A/cm^2 at 0 V bias, a peak R of 0.43 A/W, a peak D^* of 2.46×10^{11} Jones, and a rapid response time of 22.4 μs, which are much higher than PD based on the $CsPbIBr_2$ perovskite. The mechanism underlying the performance enhancement of the self-powered $CsI(PbBr_2)_{0.99}(AgI)_{0.01}$ perovskite PD was explored and attributed to the improved surface morphology and reduced recombination of the photogenerated carriers. Our work provides a promising route for developing high-performing self-powered PD for sensing applications in structural health monitoring, biomedical imaging, and optical communication.

■ ASSOCIATED CONTENT

Supporting Information

The Supporting Information is available free of charge at https://pubs.acs.org/doi/10.1021/acs.jpcc.0c04144.

> Tauc plot of the $CsPbIBr_2$ and $CsI(PbBr_2)_{0.99}(AgI)_{0.01}$ perovskite films, schematic illustration of the growth mechanism of the $CsI(PbBr_2)_{0.99}(AgI)_{0.01}$ perovskite film, dark current density statistical plot of the eight measured devices for the $CsPbIBr_2$ and $CsI(PbBr_2)_{0.99}(AgI)_{0.01}$ perovskite PDs, summary of the EIS spectra parameters analyzed with fitting the Nyquist plots, trap-filled voltage and trap density values of the $CsPbIBr_2$ and $CsI(PbBr_2)_{0.99}(AgI)_{0.01}$ perovskite photodetectors (PDF)

■ AUTHOR INFORMATION

Corresponding Author

Okenwa I. Okoli − *High-Performance Materials Institute, FAMU-FSU College of Engineering, Tallahassee, Florida 32310, United States;* orcid.org/0000-0003-1918-6442; Email: okoli@eng.famu.fsu.edu

Authors

Vincent Obiozo Eze − *High-Performance Materials Institute, FAMU-FSU College of Engineering, Tallahassee, Florida 32310, United States;* orcid.org/0000-0001-9875-166X

Geoffrey Ryan Adams − *High-Performance Materials Institute, FAMU-FSU College of Engineering, Tallahassee, Florida 32310, United States;* orcid.org/0000-0003-1484-2922

Lucas Braga Carani − *High-Performance Materials Institute, FAMU-FSU College of Engineering, Tallahassee, Florida 32310, United States*

Ryan James Simpson − *High-Performance Materials Institute, FAMU-FSU College of Engineering, Tallahassee, Florida 32310, United States*

Complete contact information is available at: https://pubs.acs.org/10.1021/acs.jpcc.0c04144

Notes

The authors declare no competing financial interest.

■ ACKNOWLEDGMENTS

The authors thank Dr. Biwu Ma and his student Maya Chaaban in the Department of Chemistry, FSU, for performing the PL and TRPL measurements. The authors also thank Dr. Seigriest for the XRD measurements, Dr. Hanson's group for the EIS measurements, and Frank Allen for proofreading this paper. The funding for this work was provided by the NSF award nos. 1359235 and NSF/DMR-1644779.

■ REFERENCES

(1) Bao, C.; Yang, J.; Bai, S.; Xu, W.; Yan, Z.; Xu, Q.; Liu, J.; Zhang, W.; Gao, F. High Performance and Stable All-Inorganic Metal Halide Perovskite-Based Photodetectors for Optical Communication Applications. *Adv. Mater.* **2018**, *30*, No. 1803422.

(2) Liu, C.; Wang, K.; Yi, C.; Shi, X.; Du, P.; Smith, A. W.; Karim, A.; Gong, X. Ultrasensitive Solution-Processed Perovskite Hybrid Photodetectors. *J. Mater. Chem. C* **2015**, *3*, 6600−6606.

(3) Peng, W.; Wang, X.; Yu, R.; Dai, Y.; Zou, H.; Wang, A. C.; He, Y.; Wang, Z. L. Enhanced Performance of a Self-Powered Organic/Inorganic Photodetector by Pyro-Phototronic and Piezo-Phototronic Effects. *Adv. Mater.* **2017**, *29*, No. 1606698.

(4) Li, C.; Han, C.; Zhang, Y.; Zang, Z.; Wang, M.; Tang, X.; Du, J. Enhanced Photoresponse of Self-Powered Perovskite Photodetector Based on Zno Nanoparticles Decorated $CsPbBr_3$ Films. *Sol. Energy Mater. Sol. Cells* **2017**, *172*, 341−346.

(5) Downs, C.; Vandervelde, T. E. Progress in Infrared Photodetectors since 2000. *Sensors* **2013**, *13*, 5054−5098.

(6) Yang, J.; Bao, C.; Ning, W.; Wu, B.; Ji, F.; Yan, Z.; Tao, Y.; Liu, J. M.; Sum, T. C.; Bai, S.; et al. Stable, High-Sensitivity and Fast-Response Photodetectors Based on Lead-Free Cs2AgBiBr$_6$ Double Perovskite Films. *Adv. Opt. Mater.* **2019**, *7*, No. 1801732.

(7) Adams, G. R.; Adhikari, N.; Parker, H.; Okoli, O. Flexible Wire-Shaped Perovskite Photodetector Via Joule Heating for Improved Crystallization and Performance. *Adv. Mater. Interfaces* **2018**, No. 1800082.

(8) Meng, L.; You, J.; Yang, Y. Addressing the Stability Issue of Perovskite Solar Cells for Commercial Applications. *Nat. Commun.* **2018**, *9*, No. 5265.

(9) Li, Y.; Shi, Z.-F.; Li, S.; Lei, L.-Z.; Ji, H.-F.; Wu, D.; Xu, T.-T.; Tian, Y.-T.; Li, X.-J. High-Performance Perovskite Photodetectors Based on Solution-Processed All-Inorganic Cspbbr 3 Thin Films. *J. Mater. Chem. C* **2017**, *5*, 8355−8360.

(10) Liu, H.; Zhang, X.; Zhang, L.; Yin, Z.; Wang, D.; Meng, J.; Jiang, Q.; Wang, Y.; You, J. A High-Performance Photodetector Based on an Inorganic Perovskite−Zno Heterostructure. *J. Mater. Chem. C* **2017**, *5*, 6115−6122.

(11) Yantara, N.; Bhaumik, S.; Yan, F.; Sabba, D.; Dewi, H. A.; Mathews, N.; Boix, P. P.; Demir, H. V.; Mhaisalkar, S. Inorganic Halide Perovskites for Efficient Light-Emitting Diodes. *J. Phys. Chem. Lett.* **2015**, *6*, 4360−4364.

(12) Du, Z.; Fu, D.; Yang, T.; Fang, Z.; Liu, W.; Gao, F.; Wang, L.; Yang, Z.; Teng, J.; Zhang, H.; Yang, W. Photodetectors with Ultra-High Detectivity Based on Stabilized All-Inorganic Perovskite $CsPb_{0.922}Sn_{0.078}I_3$ Nanobelts. *J. Mater. Chem. C* **2018**, *6*, 6287−6296.

(13) Xue, M.; Zhou, H.; Ma, G.; Yang, L.; Song, Z.; Zhang, J.; Wang, H. Investigation of the Stability for Self-Powered Cspbbr3 Perovskite Photodetector with an All-Inorganic Structure. *Sol. Energy Mater. Sol. Cells* **2018**, *187*, 69−75.

(14) Cen, G.; Liu, Y.; Zhao, C.; Wang, G.; Fu, Y.; Yan, G.; Yuan, Y.; Su, C.; Zhao, Z.; Mai, W. Atomic-Layer Deposition-Assisted Double-Side Interfacial Engineering for High-Performance Flexible and Stable $CsPbBr_3$ Perovskite Photodetectors toward Visible Light Communication Applications. *Small* **2019**, *15*, No. 1902135.

(15) Zhou, H.; Song, Z.; Grice, C. R.; Chen, C.; Zhang, J.; Zhu, Y.; Liu, R.; Wang, H.; Yan, Y. Self-Powered $CsPbBr_3$ Nanowire

Photodetector with a Vertical Structure. *Nano Energy* **2018**, *53*, 880−886.

(16) Zhou, H.; Zeng, J.; Song, Z.; Grice, C. R.; Chen, C.; Song, Z.; Zhao, D.; Wang, H.; Yan, Y. Self-Powered All-Inorganic Perovskite Microcrystal Photodetectors with High Detectivity. *J. Phys. Chem. Lett.* **2018**, *9*, 2043−2048.

(17) Li, W.; Rothmann, M. U.; Liu, A.; Wang, Z.; Zhang, Y.; Pascoe, A. R.; Lu, J.; Jiang, L.; Chen, Y.; Huang, F.; et al. Phase Segregation Enhanced Ion Movement in Efficient Inorganic Cspbibr2 Solar Cells. *Adv. Energy Mater.* **2017**, *7*, No. 1700946.

(18) Zhang, B.; Bi, W.; Wu, Y.; Chen, C.; Li, H.; Song, Z.; Dai, Q.; Xu, L.; Song, H. High-Performance $CsPbIBr_2$ Perovskite Solar Cells: Effectively Promoted Crystal Growth by Antisolvent and Organic Ion Strategies. *ACS Appl. Mater. Interfaces* **2019**, *11*, 33868−33878.

(19) Zhu, W.; Zhang, Q.; Chen, D.; Zhang, Z.; Lin, Z.; Chang, J.; Zhang, J.; Zhang, C.; Hao, Y. Intermolecular Exchange Boosts Efficiency of Air-Stable, Carbon-Based All-Inorganic Planar Cspbibr2 Perovskite Solar Cells to over 9%. *Adv. Energy Mater.* **2018**, *8*, No. 1802080.

(20) Li, B.; Zhang, Y.; Fu, L.; Yu, T.; Zhou, S.; Zhang, L.; Yin, L. Surface Passivation Engineering Strategy to Fully-Inorganic Cubic Cspbi 3 Perovskites for High-Performance Solar Cells. *Nat. Commun.* **2018**, *9*, No. 1076.

(21) Eze, V. O.; Lei, B.; Mori, T. Air-Assisted Flow and Two-Step Spin-Coating for Highly Efficient Ch3nh3pbi3 Perovskite Solar Cells. *Jpn. J. Appl. Phys.* **2016**, *55*, No. 02BF08.

(22) Eze, V. O.; Mori, T. Enhanced Photovoltaic Performance of Planar Perovskite Solar Cells Fabricated in Ambient Air by Solvent Annealing Treatment Method. *Jpn. J. Appl. Phys.* **2016**, *55*, No. 122301.

(23) Ogunsolu, O. O.; Murphy, I. A.; Wang, J. C.; Das, A.; Hanson, K. Energy and Electron Transfer Cascade in Self-Assembled Bilayer Dye-Sensitized Solar Cells. *ACS Appl. Mater. Interfaces* **2016**, *8*, 28633−28640.

(24) Ogunsolu, O. O.; Wang, J. C.; Hanson, K. Inhibiting Interfacial Recombination Events in Dye-Sensitized Solar Cells Using Self-Assembled Bilayers. *ACS Appl. Mater. Interfaces* **2015**, *7*, 27730−27734.

(25) Shahbazi, S.; Tsai, C.-M.; Narra, S.; Wang, C.-Y.; Shiu, H.-S.; Afshar, S.; Taghavinia, N.; Diau, E. W.-G. Ag Doping of Organometal Lead Halide Perovskites: Morphology Modification and P-Type Character. *J. Phys. Chem. C* **2017**, *121*, 3673−3679.

(26) Chen, L.; Wan, L.; Li, X.; Zhang, W.; Fu, S.; Wang, Y.; Li, S.; Wang, H.-Q.; Song, W.; Fang, J. Inverted All-Inorganic $CsPbI_2Br$ Perovskite Solar Cells with Promoted Efficiency and Stability by Nickel Incorporation. *Chem. Mater.* **2019**, *31*, 9032−9039.

(27) Liang, J.; Liu, Z.; Qiu, L.; Hawash, Z.; Meng, L.; Wu, Z.; Jiang, Y.; Ono, L. K.; Qi, Y. Enhancing Optical, Electronic, Crystalline, and Morphological Properties of Cesium Lead Halide by Mn Substitution for High-Stability All-Inorganic Perovskite Solar Cells with Carbon Electrodes. *Adv. Energy Mater.* **2018**, *8*, No. 1800504.

(28) Chen, Q.; Chen, L.; Ye, F.; Zhao, T.; Tang, F.; Rajagopal, A.; Jiang, Z.; Jiang, S.; Jen, A. K.-Y.; Xie, Y.; et al. Ag-Incorporated Organic−Inorganic Perovskite Films and Planar Heterojunction Solar Cells. *Nano Lett.* **2017**, *17*, 3231−3237.

(29) Kato, Y.; Ono, L. K.; Lee, M. V.; Wang, S.; Raga, S. R.; Qi, Y. Silver Iodide Formation in Methyl Ammonium Lead Iodide Perovskite Solar Cells with Silver Top Electrodes. *Adv. Mater. Interfaces* **2015**, *2*, No. 1500195.

(30) Guo, Y.; Yin, X.; Liu, J.; Que, W. Highly Efficient $CsPbIBr_2$ Perovskite Solar Cells with Efficiency over 9.8% Fabricated Using a Preheating-Assisted Spin-Coating Method. *J. Mater. Chem. A* **2019**, *7*, 19008−19016.

(31) Eze, V. O.; Seike, Y.; Mori, T. Efficient Planar Perovskite Solar Cells Using Solution-Processed Amorphous WOx/Fullerene C_{60} as Electron Extraction Layers. *Org. Electron.* **2017**, *46*, 253−262.

(32) Lei, B.; Eze, V. O.; Mori, T. High-Performance $CH_3NH_3PbI_3$ Perovskite Solar Cells Fabricated under Ambient Conditions with High Relative Humidity. *Jpn. J. Appl. Phys.* **2015**, *54*, No. 100305.

(33) Lei, B.; Eze, V. O.; Mori, T. Effect of Morphology Control of Light Absorbing Layer on Ch3nh3pbi3 Perovskite Solar Cells. *J. Nanosci. Nanotechnol.* **2016**, *16*, 3176−3182.

(34) Wang, K.; Lin, Z.; Ma, J.; Liu, Z.; Zhou, L.; Du, J.; Chen, D.; Zhang, C.; Chang, J.; Hao, Y. High-Performance Simple-Structured Planar Heterojunction Perovskite Solar Cells Achieved by Precursor Optimization. *ACS Omega* **2017**, *2*, 6250−6258.

(35) Fan, L.; Liu, S.; Lei, Y.; Qi, R.; Guo, L.; Yang, X.; Meng, Q.; Dai, Q.; Zheng, Z. Unusually Dispersed Agi Quantum Dots for Efficient Htl-Free $CH_3NH_3PbI_3$ Photovoltaics. *ACS Appl. Mater. Interfaces* **2019**, *11*, 45568−45577.

(36) Siegler, T. D.; Zhang, Y.; Dolocan, A.; Reimnitz, L. C.; Torabi, A.; Abney, M. K.; Choi, J.; Cossio, G.; Houck, D. W.; Yu, E. T.; et al. Addition of Monovalent Silver Cations to $CH_3NH_3PbBr_3$ Produces Crystallographically Oriented Perovskite Thin Films. *ACS Appl. Energy Mater.* **2019**, *2*, 6087−6096.

(37) Geske, T.; Li, J.; Worden, M.; Shan, X.; Chen, M.; Bade, S. G. R.; Yu, Z. Deterministic Nucleation for Halide Perovskite Thin Films with Large and Uniform Grains. *Adv. Funct. Mater.* **2017**, *27*, No. 1702180.

(38) Adams, G. R.; Eze, V. O.; Shohag, M. A. S.; Simpson, R.; Parker, H.; Okoli, O. Fabrication of Rapid Response Self-Powered Photodetector Using Solution-Processed Triple Cation Lead-Halide Perovskite. *Eng. Res. Express* **2020**, *2*, No. 015043.

(39) Li, G.; Ching, K. L.; Ho, J. Y.; Wong, M.; Kwok, H. S. Identifying the Optimum Morphology in High-Performance Perovskite Solar Cells. *Adv. Energy Mater.* **2015**, *5*, No. 1401775.

(40) Wu, W.-Q.; Chen, D.; Huang, F.; Cheng, Y.-B.; Caruso, R. A. Optimizing Semiconductor Thin Films with Smooth Surfaces and Well-Interconnected Networks for High-Performance Perovskite Solar Cells. *J. Mater. Chem. A* **2016**, *4*, 12463−12470.

(41) Zhang, W.; Saliba, M.; Moore, D. T.; Pathak, S. K.; Hörantner, M. T.; Stergiopoulos, T.; Stranks, S. D.; Eperon, G. E.; Alexander-Webber, J. A.; Abate, A. Ultrasmooth Organic−Inorganic Perovskite Thin-Film Formation and Crystallization for Efficient Planar Heterojunction Solar Cells. *Nat. Commun.* **2015**, *6*, No. 6142.

(42) Gholipour, S.; Correa-Baena, J. P.; Domanski, K.; Matsui, T.; Steier, L.; Giordano, F.; Tajabadi, F.; Tress, W.; Saliba, M.; Abate, A.; et al. Highly Efficient and Stable Perovskite Solar Cells Based on a Low-Cost Carbon Cloth. *Adv. Energy Mater.* **2016**, *6*, No. 1601116.

(43) Zhu, W.; Zhang, Z.; Chai, W.; Zhang, Q.; Chen, D.; Lin, Z.; Chang, J.; Zhang, J.; Zhang, C.; Hao, Y. Band Alignment Engineering Towards High Efficiency Carbon-Based Inorganic Planar $CsPbIBr_2$ Perovskite Solar Cells. *ChemSusChem* **2019**, *12*, 2318−2325.

(44) Dou, L.; Yang, Y. M.; You, J.; Hong, Z.; Chang, W.-H.; Li, G.; Yang, Y. Solution-Processed Hybrid Perovskite Photodetectors with High Detectivity. *Nat. Commun.* **2014**, *5*, No. 5404.

(45) Klab, T.; Luszczynska, B.; Ulanski, J.; Wei, Q.; Chen, G.; Zou, Y. Influence of Peie Interlayer on Detectivity of Red-Light Sensitive Organic Non-Fullerene Photodetectors with Reverse Structure. *Org. Electron.* **2020**, *77*, No. 105527.

(46) Donati, S. *Photodetectors: Devices, Circuits, and Applications*; IOP Publishing, 2001.

(47) Olawale, D. O.; Dickens, T.; Sullivan, W. G.; Okoli, O. I.; Sobanjo, J. O.; Wang, B. Progress in Triboluminescence-Based Smart Optical Sensor System. *J. Lumin.* **2011**, *131*, 1407−1418.

(48) Olawale, D. O.; Sullivan, G.; Dickens, T.; Tsalickis, S.; Okoli, O. I.; Sobanjo, J. O.; Wang, B. Development of a Triboluminescence-Based Sensor System for Concrete Structures. *Struct. Health Monit.* **2012**, *11*, 139−147.

(49) Rauch, T.; Böberl, M.; Tedde, S. F.; Fürst, J.; Kovalenko, M. V.; Hesser, G.; Lemmer, U.; Heiss, W.; Hayden, O. Near-Infrared Imaging with Quantum-Dot-Sensitized Organic Photodiodes. *Nat. Photonics* **2009**, *3*, 332−336.

(50) Shohag, M. A. S.; Hammel, E. C.; Olawale, D. O.; Okoli, O. O. In *Adhesive Bond Failure Monitoring with Triboluminescent Optical Fiber Sensor*, Proceedings of the SPIE 9803, Sensors and Smart Structures Technologies for Civil, Mechanical, and Aerospace

Systems, April 20, 2016; International Society for Optics and Photonics, 2016; p 98034Y.

(51) Yan, J.; Uddin, M. J.; Olawale, D. O.; Dickens, T. J.; Okoli, O. O. 3d Sensing Using Solid-State Wire-Shaped Photovoltaic Sensor in Tl-Based Structural Health Monitoring. *Triboluminescence*; Springer, 2016; pp 351−377.

(52) Kang, D. H.; Pae, S. R.; Shim, J.; Yoo, G.; Jeon, J.; Leem, J. W.; Yu, J. S.; Lee, S.; Shin, B.; Park, J. H. An Ultrahigh-Performance Photodetector Based on a Perovskite−Transition-Metal-Dichalcogenide Hybrid Structure. *Adv. Mater.* **2016**, *28*, 7799−7806.

(53) Lee, Y.; Kwon, J.; Hwang, E.; Ra, C. H.; Yoo, W. J.; Ahn, J. H.; Park, J. H.; Cho, J. H. High-Performance Perovskite−Graphene Hybrid Photodetector. *Adv. Mater.* **2015**, *27*, 41−46.

(54) Ma, C.; Shi, Y.; Hu, W.; Chiu, M. H.; Liu, Z.; Bera, A.; Li, F.; Wang, H.; Li, L. J.; Wu, T. Heterostructured Ws2/$CH_3NH_3PbI_3$ Photoconductors with Suppressed Dark Current and Enhanced Photodetectivity. *Adv. Mater.* **2016**, *28*, 3683−3689.

(55) Wang, Y.; Fullon, R.; Acerce, M.; Petoukhoff, C. E.; Yang, J.; Chen, C.; Du, S.; Lai, S. K.; Lau, S. P.; Voiry, D.; et al. Solution-Processed MoS_2/Organolead Trihalide Perovskite Photodetectors. *Adv. Mater.* **2017**, *29*, No. 1603995.

(56) Zhu, W.; Deng, M.; Chen, D.; Chen, D.; Xi, H.; Chang, J.; Zhang, J.; Zhang, C.; Hao, Y. Sacrificial Additive-Assisted Film Growth Endows Self-Powered Cspbbr 3 Photodetectors with Ultra-Low Dark Current and High Sensitivity. *J. Mater. Chem. C* **2020**, *8*, 209−218.

(57) Saidaminov, M. I.; Haque, M. A.; Almutlaq, J.; Sarmah, S.; Miao, X. H.; Begum, R.; Zhumekenov, A. A.; Dursun, I.; Cho, N.; Murali, B.; et al. Inorganic Lead Halide Perovskite Single Crystals: Phase-Selective Low-Temperature Growth, Carrier Transport Properties, and Self-Powered Photodetection. *Adv. Opt. Mater.* **2017**, *5*, No. 1600704.

(58) Zhang, Y.; Li, S.; Yang, W.; Joshi, M. K.; Fang, X. Millimeter-Sized Single-Crystal Cspbrb3/Cui Heterojunction for High-Performance Self-Powered Photodetector. *J. Phys. Chem. Lett.* **2019**, *10*, 2400−2407.

(59) Zhou, H.; Song, Z.; Grice, C. R.; Chen, C.; Yang, X.; Wang, H.; Yan, Y. Pressure-Assisted Annealing Strategy for High-Performance Self-Powered All-Inorganic Perovskite Microcrystal Photodetectors. *J. Phys. Chem. Lett.* **2018**, *9*, 4714−4719.

(60) Tian, C.; Wang, F.; Wang, Y.; Yang, Z.; Chen, X.; Mei, J.; Liu, H.; Zhao, D. Chemical Vapor Deposition Method Grown All-Inorganic Perovskite Microcrystals for Self-Powered Photodetectors. *ACS Appl. Mater. Interfaces* **2019**, *11*, 15804−15812.

(61) Chen, J.; Xu, J.; Zhao, C.; Zhang, B.; Liu, X.; Dai, S.; Yao, J. Enhanced Open-Circuit Voltage of Cs-Containing $FAPbI_3$ Perovskite Solar Cells by the Formation of a Seed Layer through a Vapor-Assisted Solution Process. *ACS Sustainable Chem. Eng.* **2019**, *7*, 3404−3413.

(62) Dualeh, A.; Moehl, T.; Tétreault, N.; Teuscher, J.; Gao, P.; Nazeeruddin, M. K.; Grätzel, M. Impedance Spectroscopic Analysis of Lead Iodide Perovskite-Sensitized Solid-State Solar Cells. *ACS Nano* **2014**, *8*, 362−373.

(63) Liu, X.; Li, J.; Liu, Z.; Tan, X.; Sun, B.; Xi, S.; Shi, T.; Tang, Z.; Liao, G. Vapor-Assisted Deposition of $CsPbIBr_2$ Films for Highly Efficient and Stable Carbon-Based Planar Perovskite Solar Cells with Superior Voc. *Electrochim. Acta* **2020**, *330*, No. 135266.

(64) Tan, X.; Liu, X.; Liu, Z.; Sun, B.; Li, J.; Xi, S.; Shi, T.; Tang, Z.; Liao, G. Enhancing the Optical, Morphological and Electronic Properties of the Solution-Processed Cspbibr2 Films by Li Doping for Efficient Carbon-Based Perovskite Solar Cells. *Appl. Surf. Sci.* **2020**, *499*, No. 143990.

(65) Guo, Y.; Yin, X.; Liu, J.; Que, W. Highly Efficient $CsPbIBr_2$ Perovskite Solar Cells with Efficiency over 9.8% Using Preheating-Assisted Spin-Coating Method. *J. Mater. Chem. A* **2019**, *7*, 19008−19016.

(66) Jiang, L. L.; Wang, Z. K.; Li, M.; Zhang, C. C.; Ye, Q. Q.; Hu, K. H.; Lu, D. Z.; Fang, P. F.; Liao, L. S. Passivated Perovskite Crystallization Via G-C3n4 for High-Performance Solar Cells. *Adv. Funct. Mater.* **2018**, *28*, No. 1705875.

(67) Yang, Z.; Surrente, A.; Galkowski, K.; Bruyant, N.; Maude, D. K.; Haghighirad, A. A.; Snaith, H. J.; Plochocka, P.; Nicholas, R. J. Unraveling the Exciton Binding Energy and the Dielectric Constant in Single-Crystal Methylammonium Lead Triiodide Perovskite. *J. Phys. Chem. Lett.* **2017**, *8*, 1851−1855.